Title

A Segmented Electric Aircraft Drivetrain Employing 10-Level Flying Capacitor Multi-Level Dual- Interleaved Power Modules

Authors

Bayliss, Roderick S., III
Iyer, Rahul K.
Liou, Richard
et al.

Publication Date

2023-05-01

Peer reviewed

Proceedings of the 38th Applied Power Electronics Conference and Exposition (APEC 2023), Orlando, FL,USA, 19-23 March, 2023

A Segmented Electric Aircraft Drivetrain Employing 10-Level Flying Capacitor Multi-Level Dual-Interleaved Power Modules

Roderick S. Bayliss III
Rahul K. Iyer
Richard Liou
R. C. N. Pilawa-Podgurski

A Segmented Electric Aircraft Drivetrain Employing 10-Level Flying Capacitor Multi-Level Dual-Interleaved Power Modules

Roderick S. Bayliss III, Rahul K. Iyer, Richard Liou, Robert C.N. Pilawa-Podgurski

Department of Electrical Engineering and Computer Sciences
University of California Berkeley
Berkeley, CA 94720, USA
E-mail: {rodbay, rkiyer, pilawa}@berkeley.edu

***Abstract*—Electric aircraft require power dense and efficient powertrains to become practical and break out of the laboratory and into the air. This work describes a full electric drivetrain, comprising six interleaved 10-level flying capacitor multi-level (FCML) dc-ac converters with high (38.4 kW/kg) specific power density and efficiency (98.95%). A global controller implements field-oriented control, and communicates through digital optical links to a local FPGA controller on each dual-interleaved FCML module (each module comprising two dc-ac converters). Successful demonstration on a full dynamometer test-bed with twin 250 kW electric aircraft machines is demonstrated, along with an active feedforward cancellation technique to reduce higher order harmonics.**

I. Introduction

Airborne transportation continues to produce large amounts of greenhouse gasses and is uniquely difficult to decarbonize compared to land-based transportation. Both the power density and efficiency requirements of the propulsion powertrain are incredibly stringent [1], requiring novel, high-performance solutions to decarbonize the space. In addition to aspirational climate goals, the aerospace industry also has large financial incentives to reduce fleet fuel usage due to both high fuel costs and supply chain concerns.

Several studies [1], [2] have provided the broader academic and industrial community power-density and efficiency targets in order to enable a new class of electrified transportation. To meet these targets, machine designs are moving towards higher speed operation to increase the motor power density [3]. Additionally, new, high-performance machines may forgo high-permeability and dense iron [4], thus reducing the machine filtering inductance. These machine characteristics and converter power density and efficiency targets constrain the power converter implementation and make a conventional two-level approach difficult, as it requires high machine inductance, or large external dv/dt limiting filter elements [5].

To achieve these step increases in power density and efficiency and effectively drive the next class of high power density machines, the FCML topology [6] presents an attractive solution. As the inductor of an N-level FCML converter sees an effective frequency that is $N-1$ times higher than the switching frequency and a switch-node amplitude that is $N-1$ times smaller than the dc bus voltage, a small LC filter can be employed with relatively low switching frequency (to keep switching losses low). This property allows a smooth, sinusoidal output to be applied to the machine terminals rather than the conventional pulse-width modulated voltage which alternates between discrete levels (e.g. 0 and V_{dc}). The sinusoidal waveform without high frequency harmonic components makes the FCML inverter suitable to drive steel-less, high-speed machines. In addition, the majority of the power processed by the converter is by capacitive energy storage rather than inductive as is done in traditional, switched inductor topologies. Since the energy density of capacitors is typically orders of magnitude larger than that of inductors [7], the passive volume is greatly reduced. The theoretical advantages of the topology have been validated in recent years by several very high performance prototypes [8]–[12] which have greatly outperformed more traditional approaches.

In this work, we demonstrate a modular multi-phase electric drivetrain, comprising 3 FCML converter modules with interleaved operation, through a combined micro-controller/FPGA hierarchical control structure. A global motor controller performs field-oriented control, and communicates through an optical fiber link to local FPGA controllers that are responsible for phase-shifted PWM generation.

II. Control and Communication

Typical aerospace power profiles require a large climb to cruise power ratio (e.g. the ARPA-E ASCEND example mission profile employs a ratio of three-to-one [1]). Given this, a segmented power processing approach where lower power modules are paralleled to achieve the peak power during takeoff presents a desirable approach. Rather than requiring a monolithic power converter to have favorable efficiency across the entire load range, each individual converter can be optimized to sacrifice light load efficiency in order to have peak efficiency at full load. On climb, all converters will operate at full load and as the total system power demand decreases, segments of the system will be turned off such that

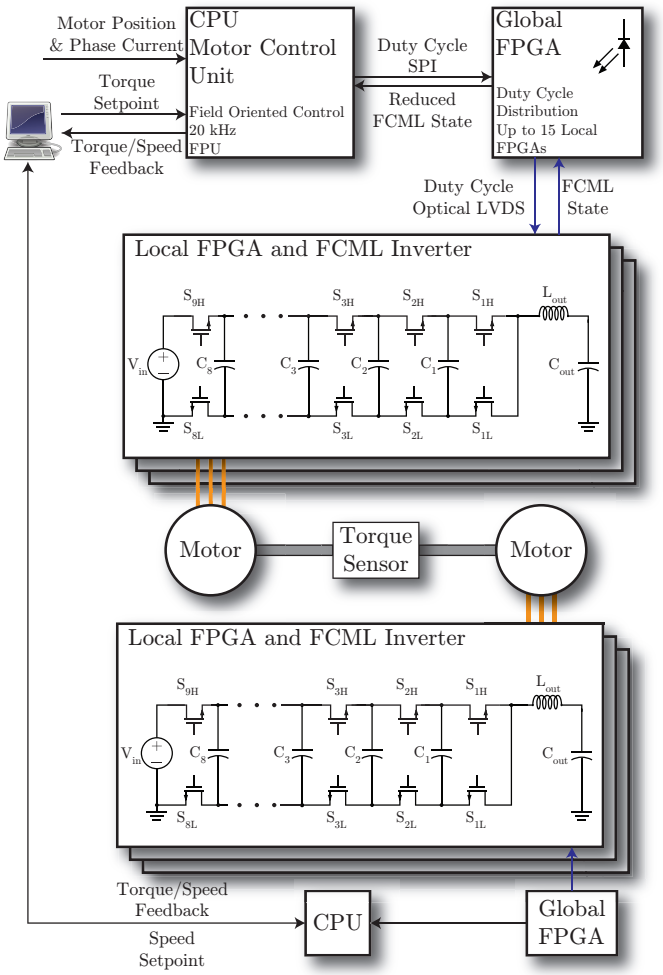

Fig. 1. Schematic of electric aircraft drivetrain employing 10-level FCML inverters in a dynamometer configuration. This figure illustrates the distribution of motor control tasks among the different compute units. Th architecture employs a C2000 microcontroller with a Floating Point Unit (FPU), enabling high performance controls and the parallelization capabilities of the FPGAs. For simplicity, only one phase of the dual-interleaved module on each interleaved module is shown.

each operating converter operates at peak efficiency. Although this segmented approach is very attractive for system power density and efficiency, it requires a judicious control and communication implementation to ensure both high level control objectives (e.g. field oriented control) and lower level actions (e.g. FCML converter commutation) work synergistically.

A. System Architecture

A diagram of the implemented control system is shown in Fig. 1. At the top level, a C2000 microcontroller is used to implement the Field Oriented Control (FOC) algorithm. The motor position and phase currents are sampled at a 20 kHz sampling frequency and the FOC algorithm employing a PI controller is executed. The C2000 microcontroller then provides duty cycle references to the global FPGA to implement the desired phase voltages. These duty cycle references

TABLE I
MAIN COMPONENTS FOR THE DRIVETRAIN AND PART NUMBERS.

Component	Part Number
C2000 microcontroller	TMS320F28379D
USB-SPI converter	FTDI FT232HL
Motor position sensor	RM44AC
Phase current sensor	LEM HO50-S
Global FPGA	10M50DAF484I7G
Local FPGA	10M16SCU169
Optical transceiver	AFBR-59F2Z
Motors	Emrax 348
Torque sensor	HBM T40B

TABLE II
INVERTER MODULE EXPERIMENTAL PERFORMANCE.

Parameter	Value
Rated DC Bus Voltage	1 kV
Effective Output Frequency	1.035 MHz
Peak Efficiency	98.95%
Peak Output Power	18.9 kW
Gravimetric Power Density	38.4 kW/kg
Volumetric Power Density	24.4 kW/L

are then parsed by the global FPGA and distributed to the downstream, local FPGAs through optical communication, which then generate the switching functions for the FCML converters. This control architecture enables the utilization of the Floating-Point Unit (FPU) and advanced analog capabilities of the C2000 and the inherent parallelization capabilities of the FPGAs. The current controller was designed to have a bandwidth of 500 Hz and the speed controller a bandwidth of 5 Hz.

To command the dynamometer system and log its reported data, the C2000 communicates through a USB-SPI converter and a standard CAN transceiver. Over the USB-SPI link, high frequency I_q and speed measurements are reported by the C2000 while the PC commands either a torque or speed set-point for the algorithm to execute. Finally, the CAN bus handles data such as dc bus voltage and input current, and motor temperatures. A visualization of the data flow within the Host PC is shown in Fig. 2. The centralization of low-level tasks within a single Python script enables automated torque-speed sweeps and efficiency maps to be performed automatically.

Annotated photographs of key system components are shown in Fig. 4 while a photograph of the FCML converter PCB is shown in Fig. 3.

III. EXPERIMENTAL SETUP

A. Hardware

A dynamometer stand was designed and manufactured to enable realistic motor load testing and flexibility in defining the operating point of the motor drive system. Shown in Fig. 4

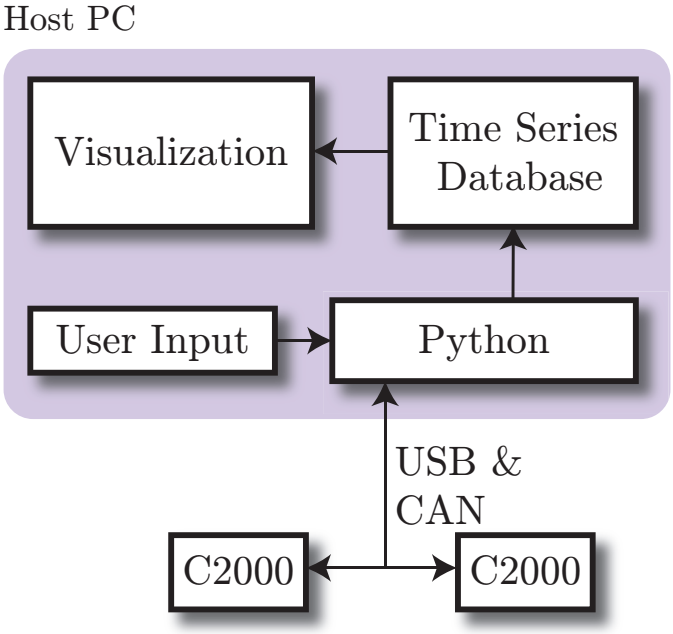

Fig. 2. Schematic elucidating data flow to and from the host PC. Within the PC the central, the Python script handles communication with the two microcontrollers by both sending current and torque setpoints over USB and monitoring the system state over both USB and CAN. This script then reports system state to a time series database (Prometheus) which interacts with a Visualization software (Grafana) for system operators to monitor the dynamometer in real time. The Python script also enables automated torque and speed sweeps and efficiency characterization.

Fig. 3. A top-down view of an InterLeaved Module (ILM). Each PCB contains two, interleaved 10-level FCML converters switching at a frequency of 115 kHz with LC filters on board. ILM electrical characteristics are given in Table II

is an annotated photograph of the realized system. Two Emrax 348s [13], axial flux permanent magnet machines, are coupled to an HBM T40B torque sensor and bolted to the floor, as a motor-generator pair. In typical operation, one of the machines is driven to operate in torque control mode while the other is driven in speed control mode. This configuration allows arbitrary selection of the operating point within the torque-speed plane and presents the power converters under test with a realistic motor load. Finally, the inclusion of the T40B torque sensor enables mechanical power and thus electrical to mechanical conversion efficiency to be obtained.

B. Adaptive Feedforward Cancellation

During initial testing, the motor control system was unable to produce a single tone phase current and instead contained a dominant fifth harmonic component. Upon further investigation, it was found this distortion was due to the flux linkage of the machine which injected a control loop disturbance. Shown in Fig. 5 is the FFT of one line-to-line voltage of the machine while being spun at a constant speed. The back emf waveform and thus flux linkage contains a sizeable fifth harmonic component, disturbing the FOC loop. Although this problem can be alleviated through an increase in control bandwidth, this approach comes with issues such as increased noise susceptibility and audible motor noise.

Following the approach in [14], an Adaptive Feedforward Cancellation (AFC) controller was implemented in conjunction with the standard FOC algorithm. If the back-emf waveform is composed of both a fundamental and 5th harmonic component, the dq components will contain both a dc and 6th harmonic term. Assuming the back-emf voltages take the following form and the machine rotates at constant speed ω.

$$v_a = f\sin(\omega t) + \sin(5\omega t) \tag{1}$$

$$v_b = f\sin(\omega t - 2\pi/3)\sin(5\omega t - 10\pi/3) \tag{2}$$

$$v_c = f\sin(\omega t + 2\pi/3) + \sin(5\omega t + 10\pi/3) \tag{3}$$

Where f is the amplitude of the fundamental component of the back-emf voltage and ωt is the position of the machine. The dq voltages can then be expressed as:

$$v_d = \frac{2}{3}\Bigg[v_a\cos(\omega t) + \left(\frac{\sqrt{3}}{2}\sin(\omega t) - \frac{\cos(\omega t)}{2}\right)v_b + \left(-\frac{\sqrt{3}}{2}\sin(\omega t) - \frac{\cos(\omega t)}{2}\right)v_c\Bigg] \tag{4}$$

$$v_q = \frac{2}{3}\Bigg[-v_a\sin(\omega t) - \left(\frac{\sqrt{3}}{2}\cos(\omega t) - \frac{\sin(\omega t)}{2}\right)v_b - \left(\frac{\sqrt{3}}{2}\cos(\omega t) - \frac{\sin(\omega t)}{2}\right)v_c\Bigg] \tag{5}$$

This equation shows that the dq voltages are created by summing the products of sinusoids in the time domain. Equivalently, these multiplications can be viewed as convolutions in the frequency domain. While the fundamental component of the abc voltages is mixed down to dc after the dq transform, the 5th harmonic component of the abc voltages creates two sidebands at $4\omega t$ and $6\omega t$. After simplification the equation for the d term results in:

$$v_d = \frac{1}{2}\Big(3\sin(6\omega t) + \sin(4\omega t) - \sin(4\omega t - \pi/3) - \sin(4\omega t + \pi/3)\Big) \tag{6}$$

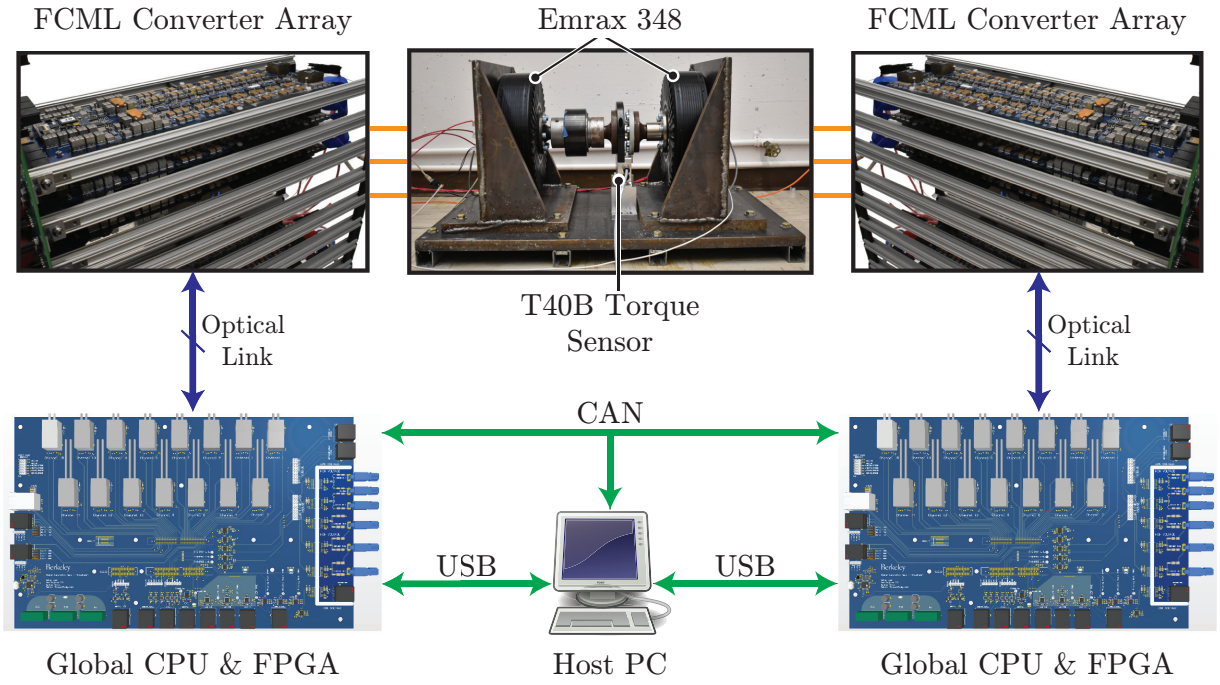

Fig. 4. Photographs of key motor drive components. The Global CPU & FPGA board connects relevant sensors (e.g. motor encoder, phase current, dc bus voltage) to the C2000 microcontroller and interconnects the FPGA and C2000 cards through two SPI links. Finally, LVDS lanes are routed from the FPGA card to the optical transceiver. Several of the FCML single phase inverters are assembled in a backplane array to form a three phase set to drive the machine. Finally, a mechanical dynamometer structure coupling two Emrax 348s and a HBM T40B torque sensor is shown in the top of the figure. The mechanical system is designed to handle the full rated torque and speed of the Emrax of 1 kNm and 4500 RPM respectively.

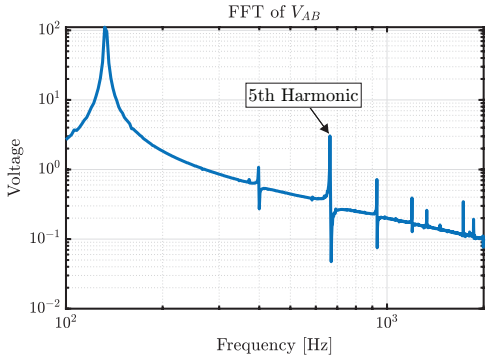

Fig. 5. FFT of a motor phase-to-phase voltage when spun at constant speed. The fundamental component dominates the spectrum of the back-emf waveform however, there is a significant fifth harmonic component which propagates as a disturbance within the FOC loop. The fifth harmonic occurs at 664 Hz for this experiment. A controller to reject this disturbance is discussed in Section III-B.

All terms at $4\omega t$ cancel and the d-axis and q-axis voltages are composed of a term at dc and $6\omega t$. This mixing property is shown graphically in Fig. 6.

The AFC controller is designed to respond to and reject only this 6th harmonic ripple in the dq reference frame by integrating the product of the error signal with a cosine at this harmonic. Thus the standard PI controller and its associated bandwidth can be maintained while the controller is able to track and reject the specific problematic harmonics. A

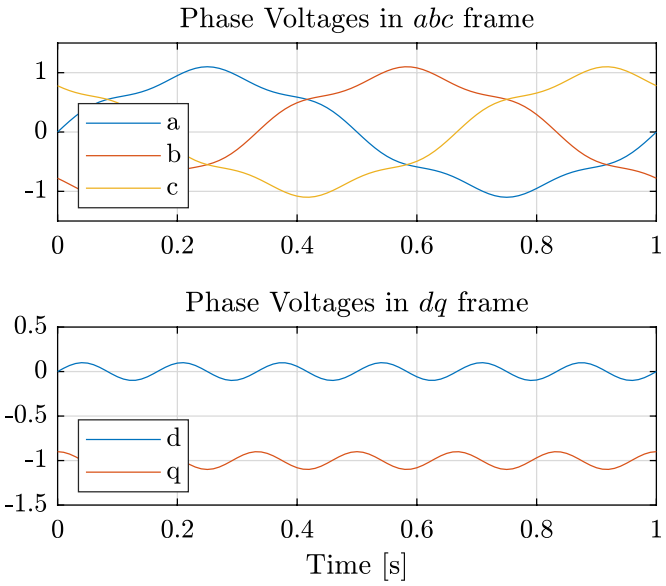

Fig. 6. Example steady-state phase voltages in a system composed of a fundamental and a non-zero 5th harmonic component where the electrical angle increases at a rate of $\omega = 2\pi$ rad/s. In this illustrative example the magnitude of the 5th harmonic is 10% of the magnitude of the fundamental. As can be seen, the fundamental component is mixed down to dc after being passed through the dq transform while the 5th harmonic is mixed up to a 6th harmonic ripple on both dq voltages.

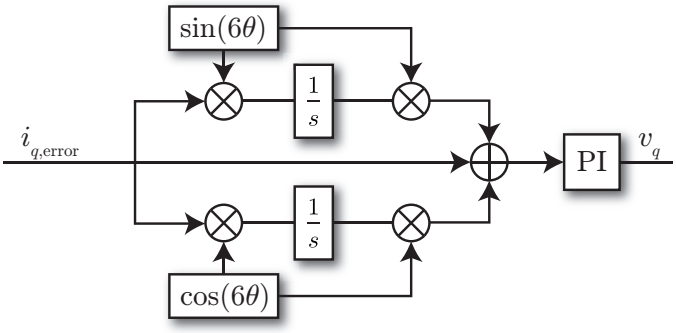

Fig. 7. Simplified block diagram of the implemented Adaptive Feedforward Cancellation (AFC) controller for the current controller for the q-axis. An identical controller is implemented for the d-axis current. The AFC controller adapts the error fed to the PI controller in order to reject the 6th harmonic current ripple induced by the fifth harmonic in the flux linkage of the machine. θ represents the electrical angle of the machine.

simplified block diagram of this control structure is shown in Fig. 7. Just like the standard FOC algorithm, this AFC controller runs on the top-level C2000 microcontroller. The efficacy of this controller is displayed in Fig. 8. After enabling the controller, the 5th harmonic current magnitude is reduced by almost 20 dB, reducing conduction losses in the machine and drive system associated with this harmonic.

IV. Conclusion

There is a clear push within both industry and academia to enable the success of electrified aircraft. Conventional approaches are likely unable to hit the requisite power density and efficiency set by system designers. By migrating to an unconventional topology such as the FCML converter, light-weight, high-speed machines can be employed with small overall system size. To validate these new techniques, this work has presented a modular multi-phase inverter drivetrain, utilizing field-oriented control on a standard microcontroller which enables realistic motor load testing of the FCML converter. Finally, this work has presented a control technique to improve the quality of the machine phase currents by rejecting periodic disturbances induced by the machine.

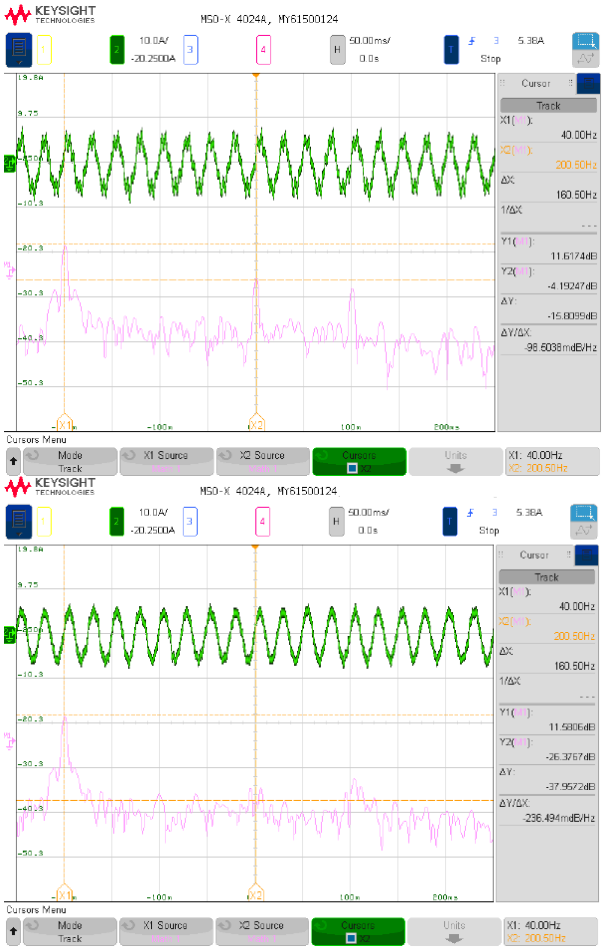

Fig. 8. Oscilloscope captures of a motor phase current measurement while the system is operating at constant speed. The top scope capture shows the system without the AFC controller enabled. The bottom subfigure shows the same conditions with the AFC controller operational. The MATH trace is the FFT of the phase current with cursors at the fundamental and the fifth harmonic. With the controller enabled, the 5th harmonic phase current magnitude has been reduced by almost 29 dB. The system operating conditions are as follows: $V_{dc} = 200$ V, $f_{\text{mechanical}} = 200$ RPM, $I_q = 5$ A.

References

[1] Advanced Research Projects Agency - Energy, "Aviation-class Synergistically Cooled Electric-motors with iNtegrated Drives." 2019. [Online]. Available: https://arpa-e-foa.energy.gov/FileContent.aspx?FileID=6506584b-87b2-4d66-8c6c-2fefcfce754f

[2] R. Jansen, G. V. Brown, J. L. Felder, and K. P. Duffy, "Turboelectric Aircraft Drive Key Performance Parameters and Functional Requirements," in *51st AIAA/SAE/ASEE Joint Propulsion Conference*. Orlando, FL: American Institute of Aeronautics and Astronautics, Jul. 2015. [Online]. Available: http://arc.aiaa.org/doi/10.2514/6.2015-3890

[3] S. Sirimanna, B. Thanatheepan, D. Lee, S. Agrawal, Y. Yu, Y. Wang, A. Anderson, A. Banerjee, and K. Haran, "Comparison of Electrified Aircraft Propulsion Drive Systems with Different Electric Motor Topologies," *Journal of Propulsion and Power*, pp. 1–15, Jun. 2021. [Online]. Available: https://arc.aiaa.org/doi/10.2514/1.B38195

[4] X. Zhang, C. L. Bowman, T. C. O'Connell, and K. S. Haran, "Large electric machines for aircraft electric propulsion," *IET Electric Power Applications*, vol. 12, no. 6, pp. 767–779, 2018. [Online]. Available: https://onlinelibrary.wiley.com/doi/abs/10.1049/iet-epa.2017.0639

[5] Y. Liu, K.-Y. See, S. Yin, R. Simanjorang, C. F. Tong, A. Nawawi, and J.-S. J. Lai, "LCL Filter Design of a 50-kW 60-kHz SiC Inverter with Size and Thermal Considerations for Aerospace Applications," *IEEE Transactions on Industrial Electronics*, vol. 64, no. 10, pp. 8321–8333, Oct. 2017.

[6] T. A. Meynard and H. Foch, "Multi-level conversion: high voltage choppers and voltage-source inverters," in *PESC '92 Record. 23rd Annual IEEE Power Electronics Specialists Conference*, Jun. 1992, pp. 397–403 vol.1.

[7] J. Zou, N. C. Brooks, S. Coday, N. M. Ellis, and R. C. Pilawa-Podgurski, "On the Size and Weight of Passive Components: Scaling Trends for High-Density Power Converter Designs," in *2022 IEEE 23rd Workshop on Control and Modeling for Power Electronics (COMPEL)*, Jun. 2022, pp. 1–7, iSSN: 1093-5142.

[8] N. Pallo, S. Coday, J. Schaadt, P. Assem, and R. C. N. Pilawa-Podgurski, "A 10-Level Flying Capacitor Multi-Level Dual-Interleaved Power Module for Scalable and Power-Dense Electric Drives," in *2020 IEEE Applied Power Electronics Conference and Exposition (APEC)*, Mar. 2020, pp. 893–898, iSSN: 2470-6647.

[9] Y. Lei, C. Barth, S. Qin, W.-C. Liu, I. Moon, A. Stillwell, D. Chou, T. Foulkes, Z. Ye, Z. Liao, and R. C. N. Pilawa-Podgurski, "A 2-kW Single-Phase Seven-Level Flying Capacitor Multilevel Inverter With an Active Energy Buffer," *IEEE Transactions on Power Electronics*, vol. 32,

no. 11, pp. 8570–8581, Nov. 2017.

[10] Z. Liao, D. Chou, K. Fernandez, Y.-L. Syu, and R. C. Pilawa-Podgurski, "Architecture and Control of An Interleaved 6-Level Bidirectional Converter With an Active Energy Buffer for Level-II Electric Vehicle Charging," in *2020 IEEE Energy Conversion Congress and Exposition (ECCE)*. Detroit, MI, USA: IEEE, Oct. 2020, pp. 4137–4142. [Online]. Available: https://ieeexplore.ieee.org/document/9236108/

[11] T. Modeer, N. Pallo, T. Foulkes, C. B. Barth, and R. C. N. Pilawa-Podgurski, "Design of a GaN-Based Interleaved Nine-Level Flying Capacitor Multilevel Inverter for Electric Aircraft Applications," *IEEE Transactions on Power Electronics*, vol. 35, no. 11, pp. 12 153–12 165, Nov. 2020.

[12] C. B. Barth, P. Assem, T. Foulkes, W. H. Chung, T. Modeer, Y. Lei, and R. C. N. Pilawa-Podgurski, "Design and Control of a GaN-Based, 13-Level, Flying Capacitor Multilevel Inverter," *IEEE Journal of Emerging and Selected Topics in Power Electronics*, vol. 8, no. 3, pp. 2179–2191, Sep. 2020.

[13] Emrax, "348 (380kW | 1000Nm)." [Online]. Available: https://emrax.com/e-motors/emrax-348/

[14] J. H. Cattell, "Adaptive feedforward cancellation viewed from an oscillator amplitude control perspective," Thesis, Massachusetts Institute of Technology, 2003. [Online]. Available: https://dspace.mit.edu/handle/1721.1/28280